ORIGINAL PAPER

Hydrothermal and soft-templating synthesis of mesoporous NiCo$_2$O$_4$ nanomaterials for high-performance electrochemical capacitors

Rui Ding · Li Qi · Mingjun Jia · Hongyu Wang

Abstract Mesoporous nickel cobaltite (NiCo$_2$O$_4$) nanoparticles were synthesized via a hydrothermal and soft-templating method through quasi-reverse-micelle mechanism. The physicochemical properties of the NiCo$_2$O$_4$ materials were characterized via X-ray diffraction, scanning electron microscopy, X-ray photoelectron spectra, and nitrogen sorption isotherms measurements. The electrochemical performances of the NiCo$_2$O$_4$ electrode were investigated by cyclic voltammetry, chronopotentiometry, and electrochemical impedance spectroscopy tests. The obtained NiCo$_2$O$_4$ materials exhibit typical mesoporous structures, with an average particle size of about 200 nm, a specific surface area of 88.63 m^2 g^{-1}, and a total pore volume of 0.337 cm^3 g^{-1}. The facile electrolytes penetration for the mesoporous structures favors high-performance of the NiCo$_2$O$_4$ electrode. The NiCo$_2$O$_4$ electrode shows a high specific capacitance (591 F g^{-1} at 1 A g^{-1}), high-rate capability (248 F g^{-1} at 20 A g^{-1}), and a good cycling behavior for tested 3,000 cycles, indicating a promising application for electrochemical capacitors.

1 Introduction

Environmental pollution, climate change, and exhaust of fossil fuels have triggered the ever-growing worldwide interest in developing sustainable and clean energy products [1, 2]. Electrochemical capacitors (ECs), as an important next generation of energy storage device, are now attracting intensive attention, mainly due to their higher power density than batteries and higher energy density than conventional dielectric capacitors [2, 3]. This property makes ECs ideal to augment traditional batteries in many different applications. However, to become primary devices for practical power supply, ECs must be developed further to improve their specific capacitance, rate capability, cycling stability, and operational safety [4].

As for high-performance ECs, it is key step to fabricate advanced electrode materials with the clean, efficient, and versatile use of energy. It has been reported that spinel nickel cobaltite (NiCo$_2$O$_4$) offers many intriguing advantages of high electrochemical activity, low-cost, abundant resources, and environmentally friendly [5, 6]. Therefore, NiCo$_2$O$_4$ material has been expected to be a promising cost-effective and scalable alternative to the state-of-art ECs material ruthenium dioxide (RuO$_2$) [7, 8]. To our knowledge, NiCo$_2$O$_4$ has become the focus candidate for ECs since the early report by Wei et al. [6].

It is noted that particle properties, such as morphology, size, porosity, etc., have a profound effect on the electrochemical performance of the materials, which is highly related with the route of material design and specific preparation method. In recent years, mesoporous materials

R. Ding (✉) · L. Qi · H. Wang (✉)
State Key Laboratory of Electroanalytical Chemistry, Changchun Institute of Applied Chemistry, Chinese Academy of Sciences, 5625 Renmin Street, Changchun 130022, China
e-mail: dingrui@ciac.jl.cn

H. Wang
e-mail: hongyuwang@ciac.jl.cn

R. Ding
Graduate University of Chinese Academy of Sciences, Beijing 100049, China

R. Ding · M. Jia
State Key Laboratory of Theoretical and Computational Chemistry, College of Chemistry, Jilin University, Changchun 130023, China

(e.g., mesoporous carbon or metal oxides) have been extensively investigated for ECs applications because of their excellent supercapacitive performance [9]. Among various mesoporous materials, mesoporous $NiCo_2O_4$ nanostructures [6, 10–13] have attracted particular interests and attentions due to their large specific capacitance, high-rate capability, and excellent cycling stability.

Soft-templating (ST) method is regarded as an effective technique to fabricate mesoporous materials, especially for mesoporous metal oxides, through the oil–water interface self-assembly processes between organic phase and inorganic precursors in certain solvents by applying various template agents including surfactants such as sodium dodecyl sulfate (SDS), cetyltrimethylammonium bromide (CTAB), dodecyl amine (DDA), etc. or Pluronics block copolymers like poly(ethylene oxide)–poly(propylene oxide)–poly(ethylene oxide) (PEO–PPO–PEO, with different forms of P123, F127, etc.). In addition, hydrothermal technique is a desirable method to fabricate functional nanomaterials for ECs due to its high temperature and pressure environments of particle growth. Therefore, combining these two techniques can be expected to obtain advanced materials for high-performance ECs.

In this work, nanostructured mesoporous $NiCo_2O_4$ materials were synthesized via a hydrothermal and ST combined method, in which SDS is chosen as the template. The physicochemical properties and electrochemical performances of the $NiCo_2O_4$ materials were characterized and investigated, respectively. The results demonstrate that the synthesized mesoporous $NiCo_2O_4$ nanomaterials exhibit high specific capacitance, high-rate performance, and good cycling behavior, indicating a promising candidate for high-performance ECs.

2 Experimental

2.1 Synthesis of materials

All the reagents used in the experiment were of analytical grade and were used without further purification. In a typical procedure, $Co(NO_3)_2 \cdot 6H_2O$ (0.6667 g), $Ni(NO_3)_2 \cdot 6H_2O$ (0.3333 g), and SDS (1.0000 g) were dissolved in deionized water (20 mL) under continuous magnetic stirring at 40 °C in a water bath for 30 min to form a homogenous solution. Then, NaOH (0.3 M, 22 mL) aqueous solution was poured into the above-generated solution with continuous magnetic stirring at 40 °C for another 30 min to form a well-mixed solution. Subsequently, the resulting solution was transferred into a Teflon-lined stainless-steel autoclave (50 mL) and heated at 140 °C for 12 h in a box oven, and next cooled naturally to the room temperature. The precipitates were collected by centrifugal

filtration, washed with distilled water and absolute ethanol several times, afterward dried at 60 °C for 12 h under vacuum condition, and finally annealed at 300 °C for 3 h in air atmosphere at a heating rate of 1 °C min^{-1} in a muffle stove to obtain the ultimate products. The material synthesis processes via a quasi-reverse-micelle mechanism (template self-assembly process) are illustrated in Scheme 1. The SDS ($C_{12}H_{25}SO_4Na$) is a typical anionic surfactant. First, the $C_{12}H_{25}SO_4^-$ anions strongly absorb the hydrated Ni^{2+} and Ni^{2+} cations as a result of electrostatic interactions, thus the quasi-reverse-micelles can be formed through the interface self-assembly processes between the soft template and inorganic precursors. Subsequently, the added OH^- anions continuously react with the hydrated Co^{2+} and Ni^{2+} cations in the reverse-micelles to form the –OH–Ni–OH–Co–OH– networks. And then, the nickel–cobalt hydroxides/SDS composite nanostructures were formed under the hydrothermal process. Finally, the SDS templates were removed by the washing and calcinations and meanwhile the mesoporous structures were generated among the $NiCo_2O_4$ nanoparticles.
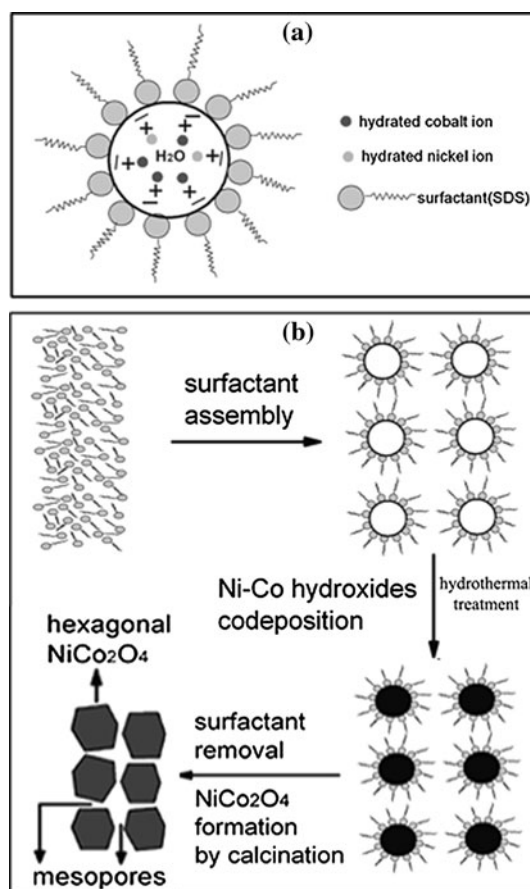
Scheme 1 Schematic representation of the mesoporous $NiCo_2O_4$ nanoparticles formation process: **a** schematic representation of a quasi-reverse-micelle, and **b** mesoporous $NiCo_2O_4$ formation process

2.2 Material characterizations

Thermogravimetry (TG) and differential thermal analysis (DTA) were carried out with a STA 449 F3 Jupiter thermogravimetric analyzer (NETZSCH) in the temperature range of 40–810 °C in air at a heating rate of 10 °C min^{-1}. X-ray diffraction (XRD) patterns were recorded on a Rigaku-Dmax 2500 diffractometer equipped with graphite monochromatized Cu Kα radiation source ($\lambda = 1.5406$ Å) at a scanning speed of 4° min^{-1} in the 2θ range of 10–80°. Scanning electron microscopy (SEM) images were conducted using Philips XL 30 and JEOL JSM-6700F microscopes. X-ray photoelectron spectra (XPS) were measured using an ESCALAB-MKII spectrometer (UK) with Al Kα radiation (1,486.6 eV) as the X-ray source for excitation, the raw spectra were curve-fitted by nonlinear least squares fittings with a Gauss–Lorentz ratio (80:20) using the XPSPEAK41 software. Surface area and porosity were determined by nitrogen sorption isotherms at 77 K using a Micromeritics ASAP 2020 Analyzer, prior to analysis, the sample was degassed under vacuum at 120 °C for 24 h. The specific surface area (SSA) was calculated using the multipoint Brunauer–Emmett–Teller (BET) method, while the pore size distribution (PSD) and pore volume data were calculated from the desorption branches of nitrogen sorption isotherms based on the Barrett–Joyner–Halenda (BJH) equation.

2.3 Electrochemical performances investigations

The electrochemical performances of NiCo$_2$O$_4$ electrode were examined by cyclic voltammetry (CV), chronopotentiometry (CP), and electrochemical impedance spectroscopy (EIS) tests, which were carried out in a conventional three-electrode electrochemical setup containing a NiCo$_2$O$_4$ working electrode (WE), a platinum plate (3 cm × 4 cm) counter electrode (CE), and a Hg/HgO (1 M KOH, aqueous) reference electrode (RE). The WE was fabricated by pressing the homogenized mixture of 66.7 wt% active material (as-synthesized NiCo$_2$O$_4$), 33.3 wt% conductive agent and binder (teflonized acetylene black, TAB; the mass ratio of AB and PTFF is 2:1) on the current collector (stainless steel mesh, 1 cm^2 area), and followed by drying in a vacuum oven at 80 °C for 12 h. The mass loading of active materials was about 4 mg cm^{-2}.

CV tests were cycled between the voltage of 0 and 0.53 V at the scan rate of 2 mV s^{-1}, CP tests were cycled between the voltage of 0 and 0.5 V with a current density range from 1 to 20 A g^{-1}, EIS experiments were taken under a constant direct current (dc) bias potential of open circuit voltage (OCV) with an alternating current (ac) amplitude of 5 mV over the sinusoidal alternating voltage frequency range of 100 kHz–10 mHz. Cycle life test was conducted via a CP measurement between the voltage of 0 and 0.5 V at the current density of 5 A g^{-1} for consecutive 3,000 cycles. The electrolytes used for tests were 6 M KOH aqueous solutions. All tests were carried out at room temperature (about 20 °C).

The gravimetric specific capacitance (C_m, F g^{-1}) and coulombic efficiency (η, %) measured from CP curves were calculated according to Eqs. (1) and (2), respectively.

$$C_m = \frac{i\Delta t_d}{\Delta V}, \tag{1}$$

$$\eta = \frac{\Delta t_d}{\Delta t_c} \times 100, \tag{2}$$

where m (g) represents the mass of active materials, i (A g^{-1}) is current density, ΔV (V) is the applied potential range, Δt_d and Δt_c are the time of discharging and charging, respectively.

3 Results and discussions

3.1 Characterizations of the NiCo$_2$O$_4$ materials

Figure 1 shows the XRD patterns of as-prepared precursors. As shown in the figure, the precursors are mainly composed of two kinds of crystalline phases of Co(OH)$_2$ (JCPDS No. 30-0443) and Ni(OH)$_2$ (JCPDS No. 74-2075) with the high crystallinity. Meanwhile, some diffraction peaks of the CoCo$_2$O$_4$ crystalline phase (JCPDS No. 80-1543) and Ni$_2$O$_3$H crystalline phase (JCPDS No. 40-1179) were detected, which is resulted from the partial oxidations of the Co(OH)$_2$ and Ni(OH)$_2$ phases in the existence of NO$_3^-$ anions under the high temperature and pressure circumstances of the hydrothermal processes. In addition, a spot of SDS signals (JCPDS No. 04-0006) were also observed, indicating the remains of the template in the precursors.
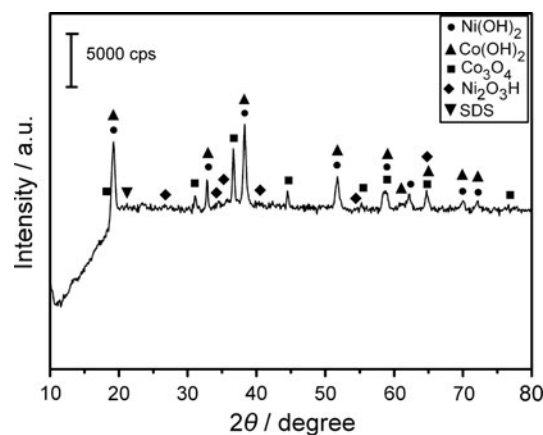

Fig. 1 XRD patterns of as-prepared precursors

TG–DTA measurements were conducted to investigate the thermal behavior of the precursor in air. As illustrated in Fig. 2a, there are three distinct weight loss steps in TG plots, corresponding to two times changes in the direction of heat flow of DTA curves which are shown in Fig. 2b. The first step (3.4 % weight loss) occurs in the temperature range between 40 and 150 °C with one DTA endothermic peak, corresponding to the evaporation of physical adsorbed water. The second step (28.6 % weight loss) occurs in the temperature range between 150 and 400 °C with two continuous but different DTA exothermic peaks (the former is short and weak, the latter is sharp and strong), which is probably caused by the difference of reaction rates during conversion process of precursor. Here, the two exothermic peaks associate with combustion of remains of surfactant template and thermal decomposition of the precursor powders to formation of $NiCo_2O_4$ spinels [14]. Note that the removal of physisorbed water and surfactant remains will open up more pore spaces and lead to larger pore volume and pore size, which favors the enhancement of porosity of the materials. The third step (8.4 % weight loss) occurs in the temperature range from 400 to 800 °C with a broad DTA endothermic peak, owing to decomposition of the $NiCo_2O_4$ spinels [15]. On the basis of the decomposition temperature range (150–400 °C) and the peak temperature value (270 °C), the temperature for calcinations was set at 300 °C for 3 h to ensure a complete decomposition of the precursor.

Figure 3 shows the XRD patterns of the $NiCo_2O_4$ materials. The resultant diffraction peaks given in the figure corroborate with the standard patterns for cubic $NiCo_2O_4$ (JCPDS No. 73-1702) with spinel structure. The sharp and well-defined diffraction lines illustrate high crystallinity of the materials. The inset of Fig. 3 shows a
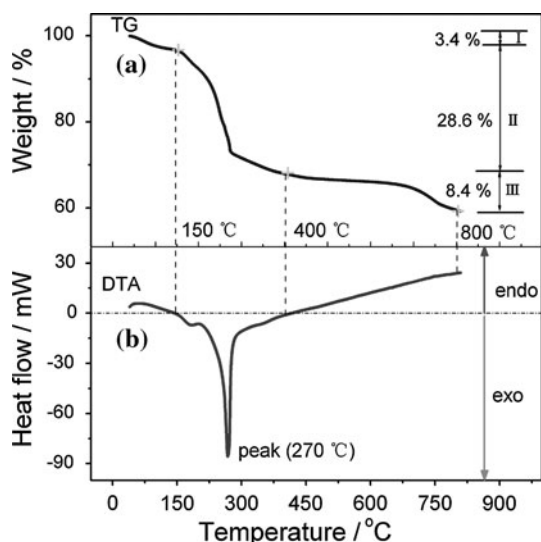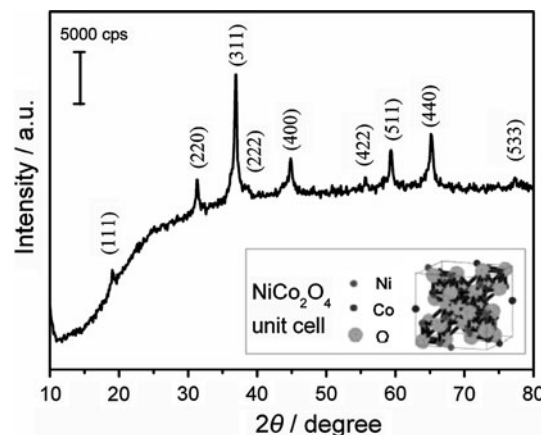

Fig. 3 XRD patterns of as-synthesized $NiCo_2O_4$ materials

picture of the $NiCo_2O_4$ spinel unit cell, the lattice parameter a_0 of the materials determined from the observed d-spacing for crystal plane (311) at 2θ value of 36.8° by using Eqs. (3) and (4), for a cubic lattice, is 0.8104 nm, basically corresponding with the standard value of 0.8110 nm for spinel $NiCo_2O_4$ (JCPDS No. 20-0781).

$$a_0 = d\left(h^2 + k^2 + l^2\right)^{\frac{1}{2}}, \tag{3}$$

$$2d\sin\theta = \lambda, \tag{4}$$

where λ is the wavelength of X-ray radiation (1.5406 Å), β is the full width at half maximum of the diffracted peak, θ is the Bragg angle of diffraction, d is observed space for crystal plane, h, k, l are the Miller indices.

The SEM images of the $NiCo_2O_4$ materials are shown in Fig. 4a–d. The observed primary $NiCo_2O_4$ particles exhibit a hexagonal morphology with diameter of ca. 200 nm. Meanwhile, there are some light aggregations which may be formed during the calcinations process, because the primary particles might sinter each other and grow into large secondary particles when calcinations [16]. However, the obtained materials still show a porous structure and this can provide easy access for ions to access the electrode/electrolyte interface, which is a very important factor for the surface Faradaic reactions.

The nitrogen adsorption–desorption isotherms, corresponding PSD and pore volume plots of the $NiCo_2O_4$ materials are shown in Fig. 5. The nitrogen sorption isotherms can be classified as type IV with a H3-type hysteresis loop according to the IUPAC classification, typical mesoporous materials. The BET SSA, BJH cumulative pore volume, and average pore diameter of the materials are 88.63 $m^2\ g^{-1}$, 0.337 $cm^3\ g^{-1}$, and 18.8 nm, respectively. Moreover, pore size exhibits a bimodal size distribution at 7.8 and 17.5 nm due to expansion of pores, indicating high porosity of the $NiCo_2O_4$ materials. Here, the not so high SSA is mainly attributed to the large particle size (200 nm),

Fig. 2 a TG and **b** DTA curves of as-prepared precursors

Fig. 4 SEM images of as-synthesized $NiCo_2O_4$ materials with different scale bars **a** 1 μm, **b** 500 nm, **c** and **d** 200 nm
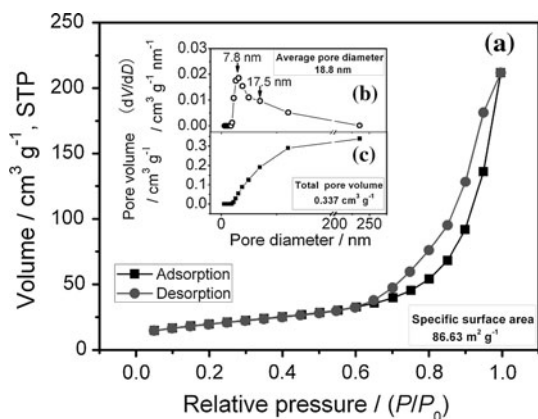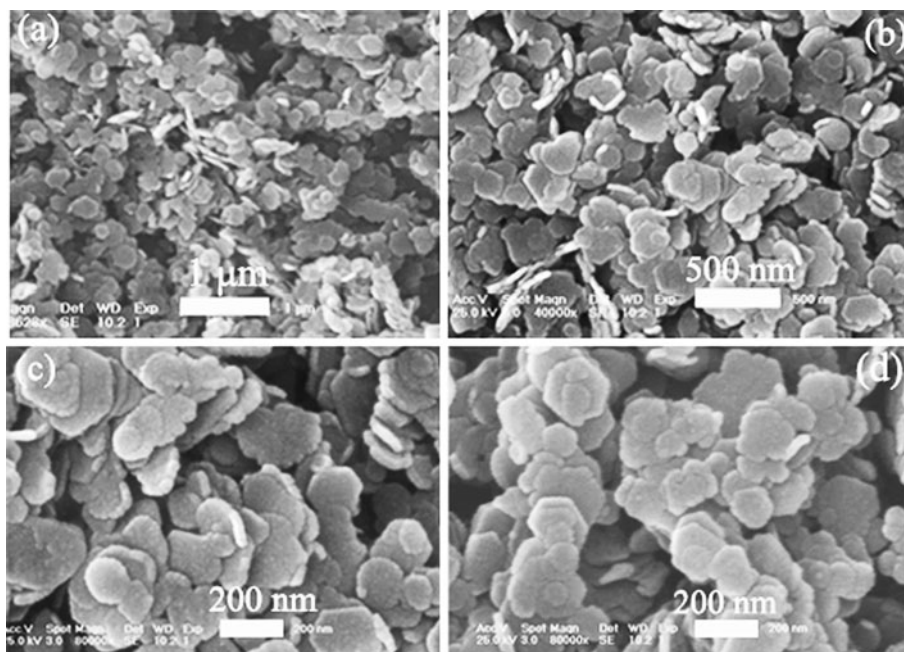

Fig. 5 **a** Nitrogen adsorption/desorption isotherms, **b** pore size distribution plots, and **c** pore volume plots of as-synthesized $NiCo_2O_4$ materials

Fig. 6 XPS profiles of as-synthesized $NiCo_2O_4$ materials: **a** survey scan, **b** O_{1s} core levels, **c** Co_{2p} core levels, and **d** Ni_{2p} core levels

and the light agglomerations of particles may cause some loss of pore volumes.

The chemical bonding states and compositions of surface elements of as-synthesized $NiCo_2O_4$ materials were evaluated by XPS which are shown in Fig. 6. It is apparent that typical signals of O_{1s}, Co_{2p}, and Ni_{2p} core levels are detected in the survey scan spectra shown in Fig. 6a. Of which, the O_{1s} spectra, as presented in Fig. 6b, show four oxygen contributions, denoted as O1 (529.3 eV), O2 (530.3 eV), O3 (531.5 eV), and O4 (532.8 eV), associating with the typical of metal–oxygen bond [17, 18], the oxygen in hydroxyl groups [19], the high number of defect sites with low-oxygen coordination in the material with small particle size [20], and the multiplicity of physi-/
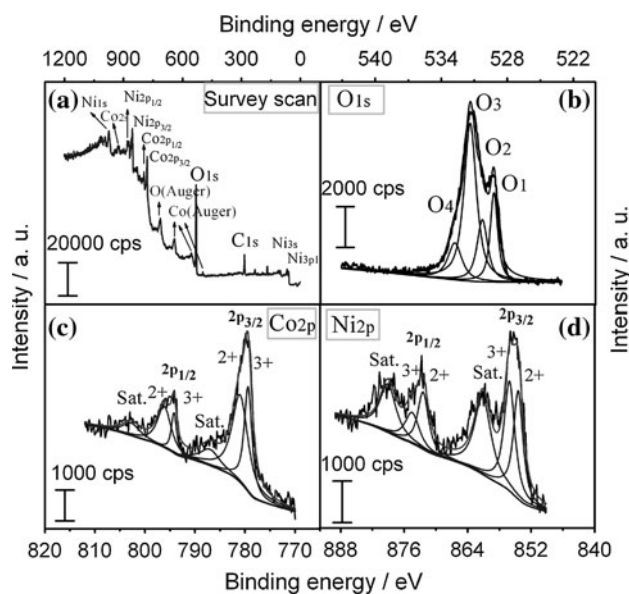
chemi-sorbed water at and within the surface [17, 18], respectively. The Co_{2p} spectra shown in Fig. 6c consist of two spin–orbit doublets characteristics of Co^{2+} and Co^{3+} and two shakeup satellites (identified as "Sat."). Similarly, the Ni_{2p} spectra given in Fig. 6d are composed of two spin–orbit doublets characteristic of Ni^{2+} and Ni^{3+} and two shakeup satellites. These results show that the surface of as-synthesized $NiCo_2O_4$ materials has a composition containing Co^{2+}, Co^{3+}, Ni^{2+}, and Ni^{3+} species. Therefore, the formula of $NiCo_2O_4$ can be generally expressed as follows:

$Co_{1-x}^{2+}Co_x^{3+}[Co^{3+}Ni_x^{2+}Ni_{1-x}^{3+}]O_4$ $(0 < x < 1)$ (the cations within the square bracket are in octahedral sites and the outside ones occupy the tetrahedral sites) [21, 22]. Here, the surface quantitative analysis of the $NiCo_2O_4$ materials based on the XPS were also conducted, which displays that the surface O/Co/Ni atomic ratio of the materials is 5.16/1.08/1, which should be 4/2/1 for the stoichiometric $NiCo_2O_4$, indicating a much enrichment in Ni species and the heavy surface non-stoichiometry of the materials, which further validates the fact that the intensity of typical of metal–oxygen bond (O1, 17.7 %) is much weaker than the sum of the oxygen in hydroxyl groups bond (O2, 17.4 %) and the high number of defect sites with low-oxygen coordination bond (O3, 51.4 %) in the O_{1s} spectra (Fig. 6b). While the some higher O atom ratio may be resulted from the absorption of physi-/chemi-sorbed water due to the capillary condensation and high surface activity of nanostructural porous $NiCo_2O_4$ materials, which corresponds to the presence of the multiplicity of physi-/chemi-sorbed water bond (O4, 13.5 %) in the O_{1s} spectra (Fig. 6b).

3.2 Investigations of the $NiCo_2O_4$ electrode

CV is a very useful tool to determine various electrode processes, electrode reaction mechanisms, electrochemical reversibility, dynamic parameters, etc. Figure 7a shows the CV plots at 2 mV s^{-1}, the whole CV plots can be divided into three electrode processes: (i) a minor electric

double-layer (EDL) process (0–0.1 V), (ii) a primary charge-transfer process (0.1–0.5 V) with one pair of broad and strong redox peaks marked as (A, C), which originates from the overall contributions of redox couples Co^{3+}/Co^{2+} and Ni^{3+}/Ni^{2+} [23, 24], (iii) a small sharp area of irreversible electrocatalytic oxygen evolution reaction process (0.5–0.53 V). Here, the electrode process is obviously dominated by the redox peaks, while the EDL occupies the much minor position, indicating the dominant Faradaic behavior of the $NiCo_2O_4$ electrode. Hence, the overall capacitance contributions of the $NiCo_2O_4$ electrode come from the minor EDL capacitance part and the major Faradaic capacity part which could be expressed as the Eq. (5) [25].

$$NiCo_2O_4 + OH^- \rightleftarrows NiCo_2O_4\|OH^- + NiCo_2O_4 - OH, \qquad (5)$$
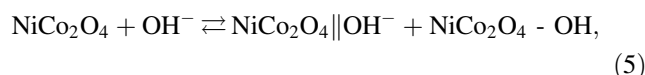
where $NiCo_2O_4\|OH^-$ represents the EDL formed by the hydroxyl ion (OH$^-$), and $NiCo_2O_4$–OH represents the product formed by oxidation reaction involving the hydroxyl ion.

Figure 7b shows the CP curves at 1–20 A g^{-1}. The charging/discharging branches present lightly asymmetric images, indicating quasi-reversible dynamics feature. Furthermore, the distinct nonlinear CP curves and obvious charging/discharging plateaus validate the dominant Faradaic behavior of the electrode, corresponding well with CV discussions. The specific capacitance and corresponding retentions under different current densities (1–20 A g^{-1}) are depicted in Fig. 7c, which exhibits a considerable specific capacitance range of 591–248 F g^{-1} and a high retention domain of 100–42 % when the current density

Fig. 7 **a** CV plots of as-fabricated $NiCo_2O_4$ electrode at a scan rate of 2 mV s^{-1}, **b** CP curves of as-fabricated $NiCo_2O_4$ electrode at different current densities (1–20 A g^{-1}), **c** specific capacitance and capacitance retention of as-fabricated $NiCo_2O_4$ electrode as a function of the current density, and **d** cycling behavior of as-fabricated $NiCo_2O_4$ electrode at a current density of 5 A g^{-1}
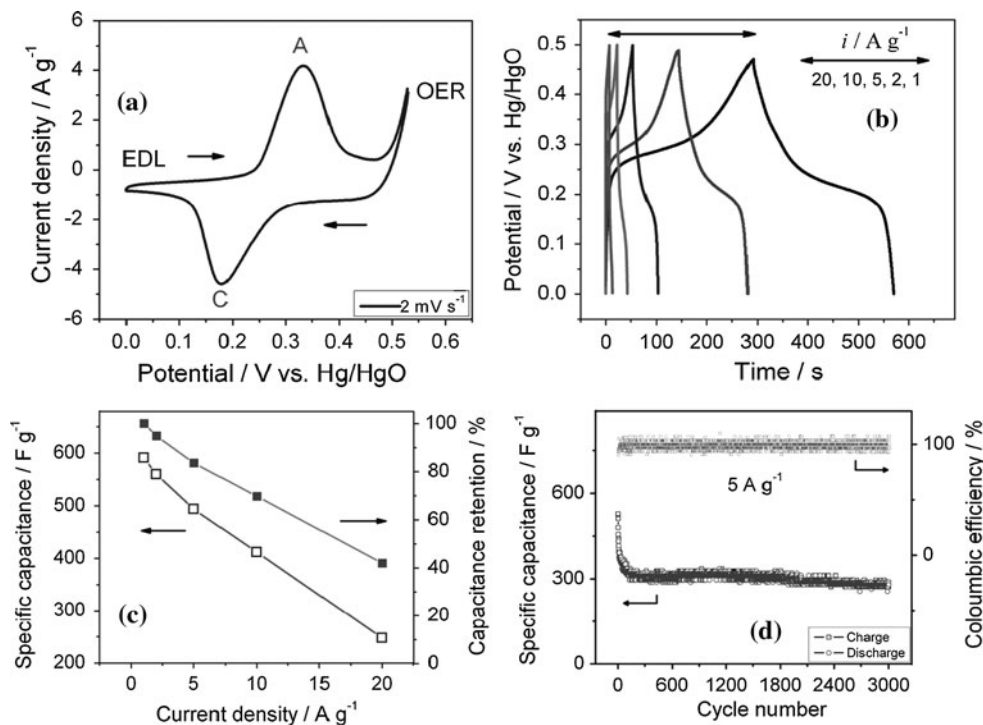
increases from 1 to 20 A g^{-1}, demonstrating the high capacitance and rate capability. The reasons for the merits of the mesoporous NiCo$_2$O$_4$ electrode may be that mesopores are capable of overcoming the primary kinetic limits of electrochemical processes [26] and make the penetration of electrolytes into the whole oxide matrix facilely and further reduce the diffusion resistance, which means that mesoporous microstructures are believed to facilitate larger capacitance and higher power rates [27].

Long cycling life is a very important factor for the electrode materials used in ECs. Figure 7d shows the cycling behavior of the NiCo$_2$O$_4$ electrode at a high-rate of 5 A g^{-1}. As demonstrated in the figure, the capacitance went through a vertical decay in the initial several cycles and then gradually decreased in the initial 100 cycles, with an obvious specific capacitance decay from 480 to 312 F g^{-1}, which is mainly resulted from the loss of irreversible energy of the NiCo$_2$O$_4$ electrode, i.e., the irreversible surface intercalation/extraction redox reactions in the lattice-embedded NiCo$_2$O$_4$ spinels. The deeper reason may be due to the heavy surface non-stoichiometry property of Co, Ni valent atoms of the materials (the intensity of metal–oxygen bond O1 (17.7 %) is much lower than the sum (68.8 %) of the high number of defect sites with low-oxygen coordination bond O3 and the oxygen in hydroxyl groups bond O2), resulting in the surface structural unstability and the irreversible surface intercalation/extraction redox reactions. Similar phenomenon has been also reported for the TiO$_2$ electrode for ECs with the LiClO$_4$ aqueous electrolytes [28], which capacity dropped sharply before 200 cycles and tended to be stable after 500 cycles, and the reason is that the percentage of surface metal–oxygen bond Ti–O–Ti (7.6 %) (Ti^{4+}) is much lower than the surface metal–hydroxyl groups bond Ti–OH (70.0 %) (Ti^{3+}) after 500 cycles, which resulted in the irreversible lithium intercalation reactions and the capacity reduction. After the initial 100 cycles, however, the NiCo$_2$O$_4$ electrode reached a much more stable state and showed a high cycling stability in the next 2,900 cycles, exhibiting 90 % retention (281 F g^{-1}) based on the value (312 F g^{-1}) of the 100th cycle. The coulombic efficiency of the electrode during all cycling periods (except the initial several cycles) maintained nearly at 100 %, showing a high coulombic efficiency under a high-rate condition. Based on the above analysis, the NiCo$_2$O$_4$ electrode exhibits a good cycling behavior, implying a promising application for the ECs.

To further investigate the electrochemical behavior of the NiCo$_2$O$_4$ electrode, EIS tests were conducted before and after 3,000 cycles. Figure 8 shows the Nyquist plots of experimental impedance data and fitted results of the NiCo$_2$O$_4$ electrode. All the measured impedance spectra are similar in shape with an arc in a higher frequency region and a spike in a lower frequency region. The

measured impedance spectra were analyzed using the complex nonlinear least-squares (CNLSs) fitting method [29] on the basis of the equivalent circuit, which is given in the inset of Fig. 8. The model circuit consists of five elements: the equivalent series resistance (R_e), the constant phase element (CPE) (Q), the charge transfer resistance (R_{ct}), the Warburg impedance (Z_W), and the limit capacitance (C_1). The R_e is a combinational resistance of ionic resistance of electrolyte, intrinsic resistance of active material, and contact resistance at the electrode/current collector interface [30]. The R_{ct}, the semicircle in the high-frequency range caused by the Faradaic reactions, represents the kinetic resistance to charge-transfer at electrode/electrolyte boundary or intrinsic charge-transfer resistance of porous electrode. The Z_W, the slope of the approximate 45° portion of the Nyquist plots in the mid-frequency range, is a result of the frequency dependence of ion diffusion/transport in the electrolyte to the bulk of electrode [31]. C_1 is the limit capacitance [29]. The CPE (Q) is used in place of double-layer capacitance (C_{dl}) at the electrode/electrolyte boundary. The impedance of CPE is defined as Eq. (6):

$$Z_{CPE} = [(Y_0 jw)^n]^{-1}, \qquad (6)$$

where Y_0 is the frequency-independent constant relating to the surface electroactive properties, w is the radial frequency, the exponent n arises from the slope of log Z versus log f (and has values $-1 \leq n \leq 1$). If $n = 0$, the CPE behaves as a pure resistor; $n = 1$, CPE behaves as a pure capacitor, $n = -1$, CPE behaves as an inductor; while $n = 0.5$ corresponds to Warburg impedance (Z_W) which is associated with the domain of mass transport control arising from the diffusion of ions to and from the electrode/electrolytes interface. The obtained values of R_e, C_{dl}, R_{ct}, Z_W, and C_1 were calculated from CNLS fitting of the experimental impedance spectra and presented in Table 1.
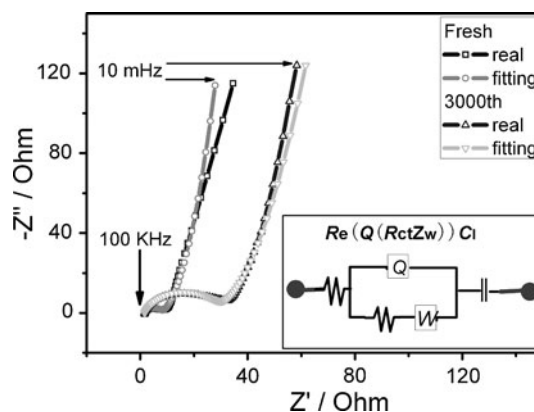

Fig. 8 Nyquist plots of experimental impedance data and fitted results of as-fabricated NiCo$_2$O$_4$ electrode in fresh and after 3,000 cycles (*inset* shows the equivalent circuit model)

Table 1 The calculated values of R_e, $Q(Y_0, n)$, R_{ct}, $Z_W(Y_0)$, and C_1 through CNLS fitting of the experimental impedance spectra based on the proposed equivalent circuit

NiCo$_2$O$_4$ electrode	R_e (Ω)	Y_0 (Ω^{-1} s^n)	n	R_{ct} (Ω)	$Z_W(Y_0)$ (Ω^{-1} s$^{0.5}$)	C_1 (F)
Fresh	1.540	5.745×10^{-4}	0.8081	6.535	0.1303	0.1427
3000th	1.599	5.159×10^{-4}	0.8093	27.40	0.07888	0.1484

The R_e, C_{dl}, and C_1 values before and after 3,000 cycles are almost the same, while a major difference comes from the R_{ct} and Z_W. After 3,000 cycles, the calculated charge-transfer resistance for the electrode is increased from 6.535 to 27.40 Ω, which is probably due to the intrinsic quasi-reversible dynamics feature of the electrode that can cause the continuous accumulations of charge-transfer resistance during the repeated charge/discharge cycling under a high-rate condition and the inevitable electrode structural deteriorations after high-rate long-term charge/discharge cycling (such as the loss of adhesion of some active materials with the current collector or the over-oxidation of current collector) that make against charge-transfer reactions. The value of Warburg resistance parameter after 3,000 cycles decreased from 0.1303 to 0.07888, which is probably due to the more generated bulk Faradaic reactions in the NiCo$_2$O$_4$ electrode that delayed the fast electrolyte ions diffusion and migration after the long-term charge/discharge cycles.

4 Conclusions

A hydrothermal and soft-templating method was exploited to fabricate mesoporous NiCo$_2$O$_4$ nanomaterials. The obtained NiCo$_2$O$_4$ materials display an average particle size of about 200 nm, a specific surface area of 88.63 m^2 g^{-1} and a total pore volume of 0.337 cm^3 g^{-1}, exhibiting typical mesoporous structures. The NiCo$_2$O$_4$ electrode shows a high specific capacitance (591 F g^{-1} at 1 A g^{-1}), high-rate capability (248 F g^{-1} at 20 A g^{-1}), and a good cycling behavior for tested 3,000 cycles, indicating a promising application for ECs.

References

1. Aricò AS, Bruce P, Scrosati B, Tarascon JM, Van Schalkwijk W (2005) Nat Mater 4:366
2. Liu C, Li F, Ma LP, Cheng HM (2010) Adv Mater 22:E28
3. Simon P, Gogotsi Y (2008) Nat Mater 7:845
4. Burke A (2000) J Power Sources 91:37
5. Cui B, Lin H, Li JB, Li X, Yang J, Tao J (2008) Adv Funct Mater 18:1440
6. Wei TY, Chen CH, Chien HC, Lu SY, Hu CC (2010) Adv Mater 22:347
7. Wang HL, Gao QM, Jiang L (2011) Small 7:2454
8. Wei TY, Chen CH, Chien HC, Lu SY, Hu CC (2009) Adv Mater 21:1
9. Liu Y, Zhao WW, Zhang XG (2008) Electrochim Acta 53:3296
10. Yuan CZ, Hou LR, Zhang XG, Shen LF, (David) Lou XW (2012) Adv Funct Mater 22:4592
11. Zhang GQ, (David) Lou XW (2013) Adv Mater 25:976
12. Zhang GQ, (David) Lou XW (2013) Sci Rep 3:1470
13. Zhang GQ, Wu HB, Hoster HE, Chan-Park MB, (David) Lou XW (2012) Energy Environ Sci 5:9453
14. Chi B, Li JB, Han YS, Chen YJ (2004) Int J Hydrog Energy 29:605
15. Peshev P, Toshev A, Gyurov G (1989) Mater Res Bull 24:33
16. Kim H, Kim YH, Joo JB, Ko JW, Yi JH (2009) Microporous Mesoporous Mater 122:283
17. Choudhury T, Saied SO, Sullivan JL, Abbot AM (1989) J Phys D 22:1185
18. Marco JF, Gancedo JR, Gracia M (2000) J Solid State Chem 153:74
19. Roginskaya YE, Morozova OV, Lubnin EN, Ulitina YE, Lopukhova GV, Trasatti S (1997) Langmuir 13:4621
20. Jimenez VM, Fernandez A, Espinos JP, Gonzalez-Elipe AR (1995) J Electron Spectrosc Relat Phenom 71:61
21. Kim JG, Pugmire DL, Battaglia D, Langell MA (2000) Appl Surf Sci 165:70
22. Zhong JH, Wang AL, Li GR, Wang JW, Ou YN, Tong YX (2012) J Mater Chem 22:5656
23. Wei TY, Chen CH, Chang KH, Lu SY, Hu CC (2009) Chem Mater 21:3228
24. Ding R, Qi L, Jia MJ, Wang HY (2012) J Appl Electrochem 42:1033
25. Choi D, Blomgren GE, Kumta PN (2006) Adv Mater 18:1178
26. Wang DW, Li F, Liu M, Lu GQ, Cheng HM (2008) Angew Chem Int Ed 47:373
27. Chang KH, Hu CC, Chou CY (2007) Chem Mater 19:2112
28. Yin J, Qi L, Wang HY (2011) ACS Appl Mater Interfaces 3:4315
29. Fabio AD, Giorgi A, Mastragostino M, Soavi F (2001) J Electrochem Soc 148:A845
30. Gamby J, Taberna PL, Simon P, Fauvarque JF, Chesneau M (2001) J Power Sources 101:109
31. Stoller MD, Park SJ, Zhu YW, An JH, Ruoff RS (2008) Nano Lett 8:3498